Characterization of a Monolithic Concatenated SOA/SA Waveguide Device for Picosecond Pulse Amplification and Shaping

Martijn J. R. Heck, *Student Member, IEEE*, Erwin A. J. M. Bente, *Member, IEEE*, Yohan Barbarin, *Student Member, IEEE*, Antigoni Fryda, *Student Member, IEEE*, Hyun-Do Jung, Yok-Siang Oei, Richard Nötzel, Daan Lenstra, *Senior Member, IEEE*, and Meint K. Smit, *Fellow, IEEE*

***Abstract*—In this paper, a monolithic waveguide device, named IRIS, is presented. The device consists of an array of concatenated semiconductor optical amplifiers and saturable absorbers. We have fabricated the devices in InP–InGaAsP bulk gain material and we have experimentally investigated picosecond pulse transmission through these devices.**

Operated as an optical amplifier the IRIS devices show a decreased temporal pulse broadening and decreased amplified spontaneous emission noise generation as compared to a semiconductor optical amplifier of equivalent length. Used as a nonlinear element to increase the optical bandwidth of a picosecond pulse train, the spectra obtained with IRIS devices show an increased broadening and smoothness as compared to a semiconductor optical amplifier.

We have set up a theoretical model to describe spectral and temporal pulse shaping by the IRIS device. Agreement between the simulations and the experiments is obtained.

***Index Terms*—Integrated optoelectronics, optical pulse amplifiers, optical pulse shaping, semiconductor optical amplifiers (SOAs), ultrafast optics.**

I. Introduction

TRAINS of short optical pulses with a wavelength around 1550 nm have many applications. Picosecond optical pulse trains can be used in telecommunications for time-domain multiplexing (TDM) systems and as synchronized multiwavelength pulse trains in wavelength division multiplexing (WDM) systems [1]. More advanced telecommunication coding technologies such as optical code-division multiple-access (O-CDMA), also make use of short optical pulses [2]. Other applications are found when the pulse train is used as a coherent optical frequency comb, e.g., in optical frequency metrology [3]. Such an optical frequency comb can also be used for arbitrary waveform generation [4].

Hybrid or monolithic integration of short pulse generation and processing systems on an optical chip offers advantages over bulk and fiber optics systems for applications as mentioned above. An optical chip is more stable and compact and can in principle be mass-produced, thus reducing fabrication costs and opening up new application areas of short pulse laser technology. These features are for example essential for reliable and cost effective implementation in future O-CDMA systems [2].

The material of choice for such optical chips operating in the 1.55-μm wavelength region is InP–InGaAsP. In this material system semiconductor mode-locked lasers can be fabricated to generate a train of short optical pulses [5]–[9]. Semiconductor optical amplifiers (SOAs) are commonly used for on-chip pulse amplification, though at the expense of adding noise to the signal in the form of amplified spontaneous emission (ASE). In [10] we proposed the use of a concatenated array of SOAs and saturable absorbers (SAs), named IRIS (Integration of Regeneration, Isolation and Spectral shaping), for further on-chip pulse train amplification and spectral shaping of these pulses. The interplay between the SOAs and SAs limits the temporal broadening of the pulses in the amplification process. Moreover the fast recovery of the SAs makes them act as gates, closing after the pulse passage and suppressing the generation of ASE. Simulations of such devices using parameters representative for InP–InGaAsP bulk gain material showed the theoretical feasibility to achieve significantly improved performance when compared to a single SOA. Depending on the operation conditions of the device, an increase in pulse peak power amplification and/or an increase of the spectral broadening can be achieved.

In this work we report on the fabrication and characterization of these IRIS devices. We focus on the amplification of a train of picosecond optical pulses and the related temporal and spectral shaping of these pulses. As we foresee a main application of the IRIS device in the combination with a semiconductor mode-locked laser, the input pulse parameters are chosen to be representative for the output pulses of these lasers. As a reference we will compare the results obtained with the IRIS devices with those obtained with an SOA of the same length. Note that SOA structures can be optimized specifically for the applications discussed. A full and extensive comparison of optimized SOA structures with the IRIS devices is beyond the scope of

Manuscript received June 26, 2007; revised November 13, 2007. This work was supported in part by the Netherlands Foundation of Scientific Research (NWO), in part by the Technology Foundation STW, in part by the Dutch Ministry of Economic Affairs through the NRC Photonics Grant through the "Towards Freeband Communication Impulse" technology program, and in part by the COST 288 action.

M. J. R. Heck, E. A. J. M. Bente, A. Fryda, H.-D. Jung, Y. S. Oei, R. Nötzel, and M. K. Smit are with the COBRA Research Institute, Eindhoven University of Technology, Eindhoven 5600 MB, The Netherlands (e-mail: m.heck@tue.nl; e.a.j.m.bente@tue.nl; h.d.jung@tue.nl; y.s.oei@tue.nl; r.noetzel@tue.nl; mk.smit@tue.nl).

Y. Barbarin was with the COBRA Research Institute, Eindhoven University of Technology, Eindhoven 5600 MB, The Netherlands. He is now with ETH Zürich, CH-8093 Zürich, Switzerland (e-mail: barbarin@phys.ethz.ch).

D. Lenstra was with the COBRA Research Institute, Eindhoven University of Technology, Eindhoven 5600 MB, The Netherlands. He is now with the Department of Electrical Engineering, Mathematics and Computer Science, Delft University of Technology, 2628 CD Delft, The Netherlands (e-mail: d.lenstra@tudelft.nl).

Digital Object Identifier 10.1109/JQE.2007.914764

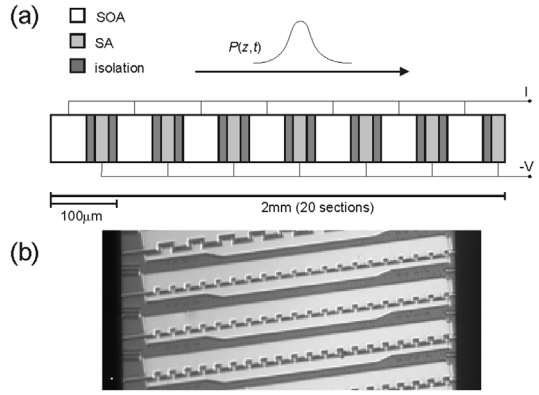

Fig. 1. (a) Schematic overview of an IRIS configuration with 20 sections used in the simulations and measurements. An input pulse (denoted by $P\ (z,t)$) enters from the left side, starting with an SOA, and exiting from the right-hand side. The ratio of the SOA and SA length within the 100-μm section (only 7 out of 20 shown) is varied. Common contacts are used for applying the injection current I and the reverse bias V. (b) Photograph of the realized devices, showing different configurations.

this work. We have used the model as presented in [10] with a minor modification to analyze the results. We have fitted a limited number of parameters in the model to reproduce the data obtained from the fabricated devices. In this way we have obtained a design tool for future improvements.

In Section II we present the fabrication technology, structure and basic design considerations of the IRIS devices realized. The model used to simulate pulse propagation through the IRIS devices and its fitted parameters are introduced in Section III. In Section IV the characterization of the IRIS devices is presented and conclusions with respect to the temporal and spectral shaping of the picosecond pulse train are made. The paper concludes with considerations for optimized performance of IRIS configurations.

II. IRIS Device Fabrication

The IRIS devices consist of a series of equal pairs of one SOA section and one SA section, as schematically depicted in Fig. 1(a). Such devices have been realized using InP–InGaAsP bulk gain material, operating at wavelengths in the region of 1.55 μm. The active layer consists of a 120-nm-thick bulk InGaAsP layer with a bandgap corresponding to $\lambda = 1.59$ μm between two 190-nm-thick $\lambda = 1.25$ μm InGaAsP layers. This structure is covered by a 1500-nm-thick p-InP cladding layer with gradually increasing doping levels and with a 200 nm p-InGaAs contacting layer.

The devices have a total length of 2 mm. Configurations with 5, 10, and 20 SOA/SA pairs and varying length ratio between the SOA and SA have been designed and realized. The sequence of SOAs and SAs is fabricated by etching a shallow ridge waveguide of 2 μm width 100 nm into the InGaAsP layer. To create electrical isolation between the SOAs and SAs, the most highly doped part of the p-cladding layers is etched away. The isolation section between the SOA and SA has a length of 10 μm (used in devices with the shorter SAs, i.e., up to 10 μm) to 15 μm (with the longer SAs). The waveguide and isolation sections are etched using an optimized CH_4/H_2 two-step RIE dry etch process.

The structures are planarized and passivated using polyimide. Two Ti/Pt/Au metal pads alternately contact the waveguide sections to create two common contacts for the SOAs and SAs, respectively [Fig. 1(b)]. The backside of the n-InP substrate is metallized to create a common ground contact. Amplification and absorption are realized by a forward or reverse electrical bias of the diode, respectively. To suppress lasing, the waveguide is oriented at the Brewster angle for the fundamental mode with the facets which have also been antireflection (AR) coated. The metal contacts are smaller and thinner towards the input and output to ease cleaving of the devices. The fabrication technology of the IRIS device is fully compatible with the technology to fabricate semiconductor mode-locked lasers as presented in [8] and [9]. This allows for future further integration of the lasers with the IRIS device.

In this work, we focus our analysis on IRIS devices with 20 sections. SOAs of 2 mm length have been processed on the same chip. These devices also have angled AR-coated facets and are used for two purposes. The first is the comparison of the performance of an SOA of comparable length and geometry with the IRIS devices. The second is to test the SOA model and extract model parameters, as done in Section III.

III. Model for IRIS Simulation

To gain insight into the temporal and spectral pulse shaping inside the IRIS devices and to obtain a design tool for future device optimization, a model has been set up to describe pulse propagation through the fabricated IRIS devices. This rate equation model that simulates picosecond pulse propagation through the SOA and SA sections individually is presented in [10]. In the following we summarize the application of this model to the InP–InGaAsP material we have used to fabricate the IRIS devices. The SOA and SA models are discussed separately below.

A. SOA Model

Picosecond pulse propagation through an SOA is described using the rate equations presented by us in [10]. These are based on those presented by Tang and Shore [11] and have been extended with equations for the ASE field to describe gain depletion through ASE analogous to e.g., the treatment in [12], [13]. Based on the experimental observations we have extended these equations with an extra gain compression and loss term due to free-carrier absorption (FCA) in the active area. This term is often ignored [11] or taken into account into the carrier heating terms [14], [15] and linear loss terms. We have rewritten the nonlinear gain g analogous to [11], but without neglecting the FCA in the following way:

$$g = \frac{g_l - \varepsilon_3 NP - \varepsilon_2 P^2}{1 + \varepsilon_1 P}$$
$$g_l = a_N (N - N_{\rm tr}) \tag{1}$$

in which g_l is the linear gain, N the carrier density in the 120 nm active layer, $N_{\rm tr}$ the carrier density needed for transparency, a_N the differential gain and $\varepsilon_1, \varepsilon_2$, and ε_3 the nonlinear gain compression factors corresponding to carrier heating (CH),

TABLE I
SIMULATION PARAMETERS AND THEIR VALUES

Parameter	Symb.	Value	Ref.
SOA			
ASE generation	$\beta \cdot B$	10^{-18}m^3/s	fit, [12,13,22]
Width of active region	w	2.0μm	[9]
Depth of active region	d	0.12μm	[9]
Linear confinement factor	Γ	0.285	[9]
Confinement factor for TPA	Γ_2	0.5	[11]
Confinement factor for UNR	Γ'_2	0.4	[11]
Differential gain	a_N	$3.5{\cdot}10^{-20}$m^2	fit, [23]
Differential gain ASE	$a_{N,ASE}$	$2.5{\cdot}10^{-20}$m^2	fit, [13]
Carrier lifetime	τ_s	0.5ns	fit, [11]
Carrier density linewidth enhancement factor	α_N	5	fit, [11]
Temperature linewidth enhancement factor	α_T	1	fit
Coefficient for TPA	β_2	37cm/GW	[11]
Nonlinear gain refractive index	n_2	$-3.5{\cdot}10^{-16}$m^2/W	[11]
Nonlinear gain compression factor	ε_1	0.2W^{-1}	*) [11]
Nonlinear gain compression corresponding to TPA	ε_2	200W^{-2}m^{-1}	[11]
Nonlinear gain compression corresponding to FCA	ε_3	$5{\cdot}10^{-9}$ W^{-1}μm^3	fit, *)
FCA coefficient	σ_{FCA}	$3{\cdot}10^{-10}$μm^2	fit, [24]
Transparency carrier density	N_{tr}	$0.3{\cdot}10^{24}$m^{-3}	fit, [11,23]
Linear loss	α_{int}	$2.0{\cdot}10^3$m^{-1}	fit, [11,23]
SA			
Linewidth enhancement factor	α_{SA}	1	[25]
Differential absorption	$a_{N,SA}$	$40{\cdot}10^{-20}$m^2	fit, [17]
Effective carrier lifetime	τ_{SA}	10ps	[26]
Transparency carrier density	$N_{tr,SA}$	$(0–0.6){\cdot}10^{24}$m^{-3}	fit

**) As the effect of ε_1 and ε_3 is closely related, the value of ε_1 is fixed at the value in [11] and the value of ε_3 is fitted to the experimental data.*

two-photon absorption (TPA) and FCA, respectively. The pulse power is denoted by P. The total linear loss term is then

$$\alpha_{\rm tot}(N) = \alpha_{\rm int} + \sigma_{\rm FCA} \cdot N \tag{2}$$

in which $\sigma_{\rm FCA}$ is the FCA coefficient and $\alpha_{\rm int}$ represents the other passive losses, including FCA in the cladding. For the full set of propagation equations, we refer to [10].

As the application of this set of equations to InP–InGaAsP SOAs has been extensively studied and reported upon in literature, we have implemented the widely used values of the parameters as much as possible. A limited set of parameters in these equations has been fitted to the results obtained with experimental picosecond pulse propagation through a 2.0 mm SOA, fabricated in the same way as the IRIS devices, as mentioned in Section II. Table I contains a list of all parameters, the values used and whether they are literature or optimized values.

B. SA Model

To describe picosecond pulse propagation through an SA we use the rate equations presented in [10], [16], [17] and the assumptions mentioned therein. The 2 mm SOAs and IRIS devices (see Section II) offer no direct possibility for the measurement of characteristics of isolated SAs. Therefore, SAs fabricated on a different wafer with the same layerstack [18] are used for experimental characterization. These devices have been fabricated

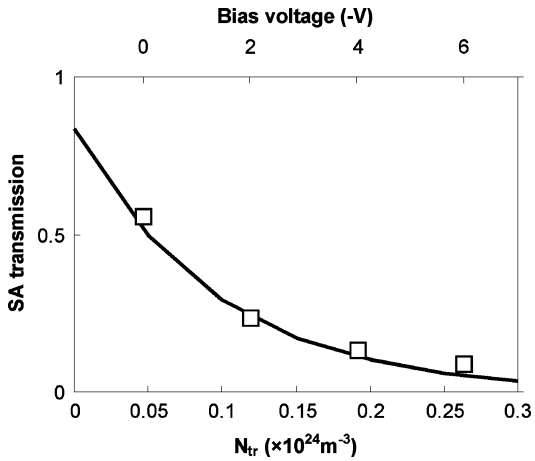

Fig. 2. Matching of the 90-μm SA transmission dependency on $N_{\rm tr}$ (line, simulation) and V (squares, experiment) for the small-signal absorption. All these experiments and simulations have been done using 1.4-ps input pulses with a repetition rate of 80 MHz and $\lambda = 1560$ nm (experiment) or single pulse transmission (simulation).

using a butt-joint active-passive integration scheme where passive waveguides guide the light to SAs that are much shorter than can be obtained by cleaving.

In SA pulse propagation models the effect of the bias voltage on the absorption is often ignored. In this work we adopt the approach of [19], where a linear dependency of the transparency carrier density in the model [10] as a function of the applied bias voltage in the experiments is proposed. We have quantified this relation and the effect on the SA transmission (absorption). These results for an SA with a length of 90 μm are shown in Fig. 2. The other SA parameters and their optimized values are given in Table I. These values have been obtained using measurement techniques as presented in [20] and [21].

To simulate a complete IRIS configuration the designed SOA lengths are used, but for the SA length they include the isolation sections (see Fig. 1). This creates an effective SA in the simulations that represents an isolation-SA-isolation section in the realized IRIS devices. In practice an isolation section is not biased, so it will act as an absorber. The field applied to the neighboring SA can penetrate into the isolation sections, effectively increasing the absorption in the isolation sections. As this effect is hard to quantify, we use this approach of a single effective SA in the simulations.

IV. IRIS CHARACTERIZATION

In this section we describe the experimental results obtained using 2-mm IRIS devices as shown in Fig. 1. In the following, picosecond pulse propagation through these devices is measured with respect to the spectral and temporal shaping of the pulses. The model and parameters for the SOA and SA from Section III are then used to investigate the experimentally obtained results. The results obtained with the IRIS devices are compared with those obtained with a 2 mm reference SOA for the applications as an amplifier and spectral shaper.

In our setup (Fig. 3) a Pritel mode-locked fiber laser (MLL) is used to generate a 10 GHz picosecond pulse train. The power and polarization of the pulses are controlled. Our devices are not packaged and lensed fibertips are used for incoupling and

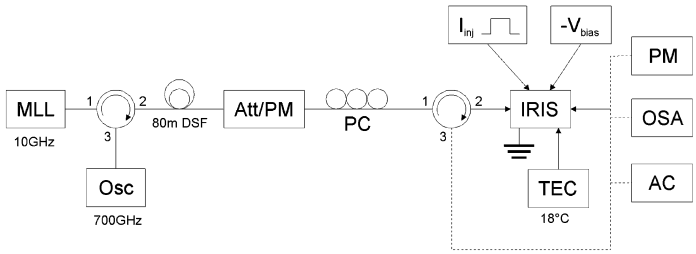

Fig. 3. Schematic overview of the setup used to characterize the SOA and IRIS devices. MLL: 10 GHz mode-locked fiber laser, Att/PM: attenuator/power meter, PC: polarization controller, TEC: thermo-electric cooler, PM: power meter, OSA: optical spectrum analyzer, AC: autocorrelator, Osc: 700 GHz optical sampling oscilloscope. All equipment is fiber pigtailed or has fiber input or output connectors. A pulsed injection current source $(\mathrm{I_{inj}})$ and voltage source $(-V_{\mathrm{bias}})$ are used to bias the SOAs and SAs, respectively.

outcoupling. Needle probes are used for biasing the contacts. The chip is held at 18 °C using a thermo-electric cooler. Pulsed injection current is used to prevent chip heating. We make use of an autocorrelator and a 700-GHz optical sampling oscilloscope for temporal pulse power profile characterization. The optical power spectrum is obtained by an optical spectrum analyzer (OSA). The MLL and optical sampling oscilloscope were located in another lab nearby. The optical signals were transported between the two labs through a total of 15-m standard single mode fiber (SMF) and 80 m of dispersion shifted fiber (DSF). The pulses at the device input have a measured duration (FWHM) of 1.4 ps and are close to transform limited (time–bandwidth product of 0.3). The pulse peak power is about 0.1 W.

For the experimental characterization we mainly focus on the IRIS devices with 20 sections for which we have obtained the most complete dataset including both time and frequency domain measurements. The SOA lengths within this set of devices are 60 μm down to 40 μm and the corresponding SA lengths are 10 μm up to 20 μm. The isolation sections between SOA and SA are 10 μm up to 15 μm, respectively. In the following the IRIS configurations will be denoted by their respective SOA and SA lengths, e.g., a 60 μm/10 μm configuration.

Operating conditions of the IRIS SOA sections are identified by the total injection current, which is assumed to be uniformly divided over the 20 SOA sections. The reverse bias voltage over the SA is simulated by scaling the transparency carrier density N_{tr} in the SA up to about $0.6{\cdot}10^{24}$ m^{-3}, where a voltage of -1 V corresponds approximately with a density of $0.05{\cdot}10^{24}$ m^{-3} $-$ $0.1 \cdot 10^{24}$ m^{-3}, as can be seen in Fig. 2.

A. IRIS Spectral Shaping

In Fig. 4(a), the measured spectra of the 1.4-ps pulse train after transmission through the IRIS device as a function of injection current are shown for three different configurations. The spectra obtained with a 2 mm SOA are given for reference. The spectra broaden with increasing injection current towards the longer wavelengths. This occurs up to a value of 400 mA, for the 10-μm SAs, or 550 mA for the 20-μm SAs. With a further increase of the injection current the broadening of the spectra remains unchanged. This is analogous to the SOA, where the broadening occurs up to a value of 300 mA.

These phenomena can be explained first by the saturation of the gain, resulting in the increase of spectral broadening towards the longer wavelengths, and secondly, for the higher currents, gain compression above the current values mentioned above. As the SAs lower the optical power of the transmitted pulse train, the gain compression takes place at a higher value of the injection current for increased SA lengths.

In Fig. 4(b), the simulated pulse spectra of a 60 μm/40 μm IRIS model configuration are shown for different values of the SA transparency carrier density. Note that the effective SA length is used in the model configurations as compared to the experimental devices, which are denoted with the SA length excluding isolation sections. From a comparison of these simulated spectra with the experimentally obtained spectra in Fig. 4(a) for the 60 μm/10 μm and 50 μm/10 μm devices, good agreement is seen for values of the transparency carrier density of 0 to $0.1 \cdot 10^{24}$ m^{-3}. As the SA bias voltage in the experiments was -1 V this is in agreement with the results as given in Fig. 2.

The simulations in Fig. 4(b) indicate that a broader and smoother spectrum can be obtained by increasing the SA bias voltage (i.e., the corresponding value of N_{tr}). More specific an increase in the red-shift can be observed of up to 8 nm for $N_{\mathrm{tr}} = 0.3 \cdot 10^{24}$ m^{-3}. A larger shift is expected for higher values of the transparency carrier density. These results would however occur at values of the injection current of over 1 A, which is beyond the scope of our analysis. Also, at lower values of the injection current and increasing with N_{tr}, an increase in blue-shift can be observed and a smooth shape of the spectrum. Such spectra thus are generated at the operating points where the SAs saturate and compress the pulses while the SOA saturation is limited. As a result the temporal broadening and the red-shift are also minimized. For a more extensive review of this subject we refer to the section below on temporal pulse shaping.

Experimentally the largest spectral broadening has been observed with the 50 μm/10 μm devices. In Fig. 4(c) we have plotted two of the measured spectra for a 50 μm/10 μm device at an injection current of 700 mA for SA bias voltages of -1 and -6 V. As can be seen the spectrum measured at FWHM broadens to over 5 nm at -6 V. Moreover the whole range of this bandwidth has a modulation depth of less than 3 dB, making the full bandwidth usable for applications such as pulse compression. This is not the case for a bias voltage of -1 V or for the 2-mm SOA, for which the spectrum is given in Fig. 4(c) for reference. Comparing these spectra to the simulated spectra in

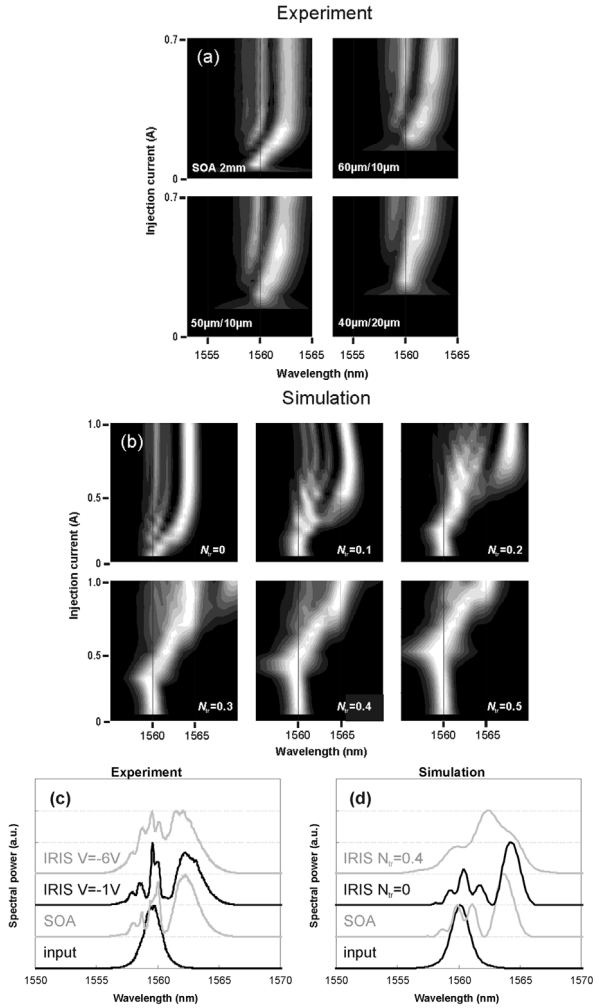

Fig. 4. (a) Experimentally obtained pulse spectra after transmission through an SOA and IRIS devices with 60 μm/10 μm, 50 μm/10 μm and 40 μm/20 μm configurations, respectively. The injection current through the SOAs is varied and $V_{\rm SA} = -1$ V. The spectra are normalized and the linear intensity scale is grey scale coded from black (0) to white (1). No spectra were recorded for the lower injection currents, hence the offset. (b) Simulated pulse spectra after transmission through a 60 μm/40 μm IRIS configuration for varying injection currents. Plots for different values of the SA transparency carrier density $N_{\rm tr}(\times 10^{24}\ {\rm m}^{-3})$ are given. (c) Experimentally obtained pulse spectra after transmission through a 50 μm/10 μm IRIS configuration for an injection current of 700 mA. The input spectrum and the SOA spectrum at an injection current of 350 mA is also given. (d) Comparison of simulated spectra for a 60 μm/40 μm configuration at an injection current of 700 mA and two values of $N_{\rm tr}$ ($\times$ 10^{24} ${\rm m}^{-3}$). The input spectrum for the simulation and the SOA spectrum at 400 mA is also shown. In both the experiments and the simulations the input pulses have a duration of 1.4 ps and a peak power of 0.1 W. The input pulse central wavelength is set to 1560 nm in the plots of the simulations to match the experimental plots.

Fig. 4(d) shows that the model correctly describes the spectral broadening. The relatively smooth spectral broadening at -6 V best corresponds to the simulated spectrum obtained for a transparency carrier density value of $0.4 \cdot 10^{24}$ ${\rm m}^{-3}$ in the model.

A comparison between the experimental and simulated spectra of Fig. 4 shows a larger shift of about 1 nm of the simulated spectra towards the longer wavelengths. This can be explained by a slight overestimation of the spectral shift in the SOA model (Section III) for higher injection currents. The SOA parameters in Table I were optimized for simulation of pulse propagation for the lower injection current regime, i.e., up to the level where gain compression takes place.

There is no significant influence of the SA recovery time in the model on the simulated spectra in the range of 5–50 ps [26]. This can be explained by the fact that the pulse repetition rate of 100 ps is far above this range and the SA can fully recover between two pulses. On the other hand the SA recovery time of over 5 ps is well beyond the pulse duration of 1–2 ps, meaning that only limited SA recovery takes place during the pulse propagation.

So concluding it can be said that the IRIS configuration shows improved spectral shaping of picosecond pulses as compared to an SOA of equivalent length. Spectral widths of over 5 nm can be obtained with a smooth shape. The useful bandwidth from the SOA stays limited to about 2 nm. This makes the spectrum suitable for use in the target applications mentioned [2], [27], [28]. Moreover the spectra obtained with our model show a quantitative agreement with the experimentally obtained spectra, making it a useful design tool. A further increase in bandwidth can be obtained at the higher injection currents, i.e., around and beyond 1 A, as can be seen in Fig. 4(b). Another working point indicated by the simulations is where the output spectra are most blue-shifted. However the total gain in these points is much below 0 dB from which we conclude that these operating points are unpractical.

B. IRIS Amplification and Noise Figure

SOAs typically add a significant amount of noise to the signal being amplified because of the ASE generated. This is especially the case when no or low-power signal is present or when the signal has a low repetition rate. As a consequence the gain is not depleted by the signal but by the ASE. High gain may be required for on-chip signal amplification. As mentioned in [29] and [30], a concatenated array of SOAs and SAs can have an S-shaped transmission curve, where lower and higher input power signals experience a lower gain than medium power signals. This feature can be used for 2R regeneration [29], [30]. In this paper, we restrict ourselves to an experimental investigation of the gain and ASE generation and its suppression in the SAs in the IRIS devices when used for amplifying a 10 GHz picosecond pulse train. We will compare the results with those from an SOA.

In Fig. 5, the S-shaped transmission is visualized by plotting the picosecond pulse train gain for two IRIS configurations with 10 SOA/SA pairs as a function of input power. Fig. 5(a) presents the measurement results from a 150 μm/10 μm device with $V_{\rm SA} = -1$ V and Fig. 5(b) presents results from a 110 μm/30 μm device with $V_{\rm SA} = -3$ V. The gain presented is defined as the total recorded output power minus the ASE floor, divided by the picosecond pulse input power. As can be seen the gain for the IRIS devices peaks at a specific input power $P_{\rm gmax}$. The value of $P_{\rm gmax}$ decreases with increasing injection currents for a specific device. The contrast in gain at low(er) input power levels and at $P_{\rm gmax}$ shows the possibility of ASE suppression while still amplifying the picosecond pulse train. Comparing the IRIS device with the shorter SAs (and $V_{\rm SA} = -1$ V) in Fig. 5(a) with the one with the longer SAs (and $V_{\rm SA} = -3$ V) in Fig. 5(b), it can be seen that the gain contrast is largest

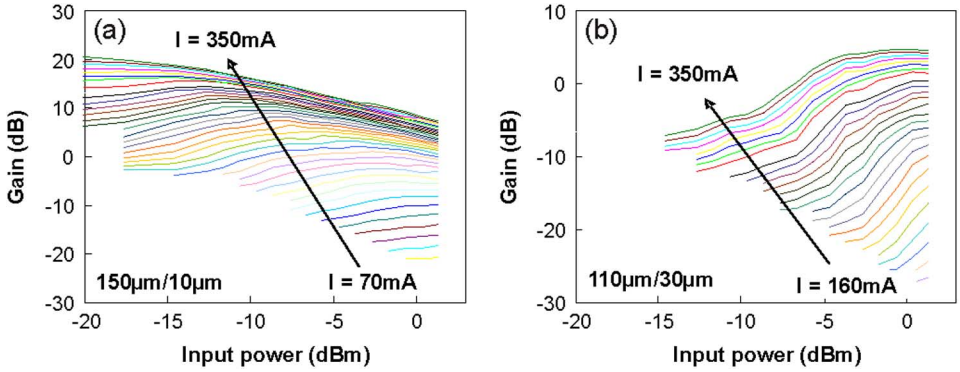

Fig. 5. On-chip gain curves for IRIS configurations with 10 SOA/SA pairs with respective lengths and reverse bias voltage of (a) 150 μm/10 μm, $V_{\rm SA} = -1$ V and (b) 110 μm/30 μm, $V_{\rm SA} = -3$ V. The injection current is increased (7.5-mA steps) from 70 mA up to 340 mA. Fiber coupling losses are estimated at 5 dB per facet. Further input pulse parameters are as in Fig. 4.

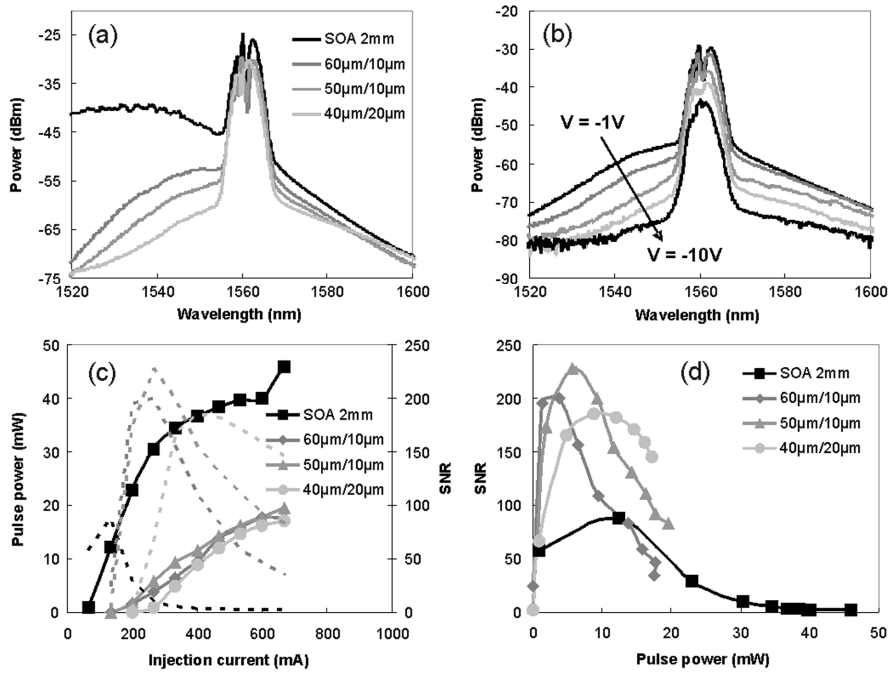

Fig. 6. (a) Output pulse spectra obtained at an injection current of 700 mA, for IRIS configurations of 60 μm/10 μm, 50 μm/10 μm and 40 μm/20 μm and with $V_{\rm SA} = -1$ V. The SOA spectrum is given for reference. (b) Output pulse spectra at 700 mA for different reverse bias voltages for a 50 μm/10 μm configuration. (c) Output pulse power (solid) and SNR (dotted) for different configurations as a function of injection current and (d) the SNR plotted versus the output pulse power.

(13 dB) for the 110 μm/30 μm device. The gain contrast for the 150 μm/10 μm device is 7 dB only. However the total device gain for the 110 μm/30 μm device is about 5 dB lower than that of the 150 μm/10 μm device. Thus, depending on the application a tradeoff has to be made between the signal gain and the contrast between the peak gain and the lower power gain.

To optimize the balance between ASE suppression and total gain, the observed device gain and ASE generation is presented in more detail in Fig. 6. The recorded optical spectra of the device output can be used to separate the power in the pulse train from the generated ASE. As can be seen in Fig. 6(a) for high injection currents (in this case $I = 700$ mA) the ASE generation is suppressed by 10 dB with respect to the SOA output near the picosecond pulse wavelength. The power in the pulse train is however only 3–5 dB lower compared to the SOA. The same effect can be observed when the reverse bias over the SA is increased [Fig. 6(b)].

By integrating the power in the spectrum over the pulse train bandwidth and the ASE bandwidth separately, the ratio of power in both fields can be determined. In this paper we define this ratio by the signal-to-noise ratio (SNR). In Fig. 6(c) the calculated pulse output power (as a measure of the gain) and the corresponding SNR are plotted. As expected the (device) gain for the reference SOA shows a sharp increase at lower injection current values as compared to the IRIS configurations (i.e., 70 mA as compared to 120 mA–200 mA for increasing SA length). The reason is the increased power (i.e., increased gain) that is necessary to saturate the SAs. The gain that can be obtained using an SOA is however only 3 dB more than that can be obtained with an IRIS device. In the SNR curves, the IRIS devices show a

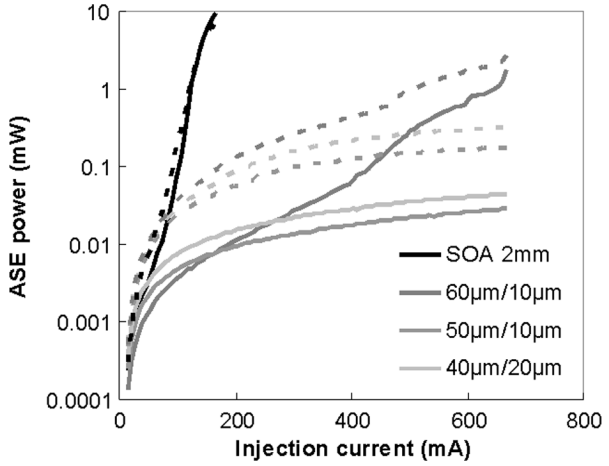

Fig. 7. *L–I* curves for the 2 mm SOA and IRIS configurations with 60 μm/10 μm, 50 μm/10 μm and 40 μm/20 μm configurations at $V_{\rm SA} = -1$ V. The solid curves represent the fiber coupled ASE at the output facet and the dotted curves the counter-propagating ASE at the input facet.

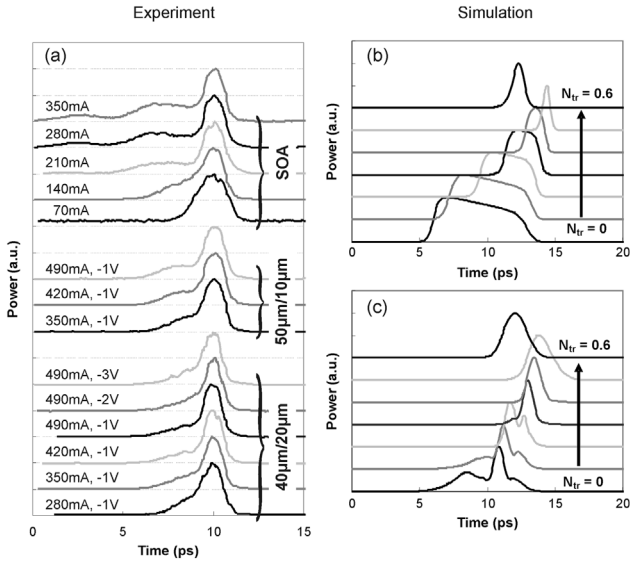

Fig. 8. (a) Normalized temporal pulse profiles after propagation through 15 m of SMF, obtained with a 700 GHz optical sampling oscilloscope. Pulse profiles obtained with IRIS configurations of 40 μm/20 μm and 50 μm/10 μm and an SOA are shown. These experimental curves have been shifted to overlap in time; absolute position measurement is not possible in our setup. Curves have been vertically offset for clarity. (b) Simulated pulse shapes for a 60 μm/40 μm configuration at the output and (c) after propagation through 15 m of SMF at an injection current of 500 mA. Traces are given for a range (0.1-steps) of SA transparency carrier densities $N_{\rm tr}(\times 10^{24}\ {\rm m}^{-3})$.

superior performance over the SOA for the higher injection currents. To make a good comparison between the IRIS device and an SOA with respect to picosecond pulse amplification and the SNR, the gain of the devices (output power) is plotted against the SNR in Fig. 6(d). As can be seen the SOA can achieve higher gain values, but at very low SNR values. For the lower values for the gain, the IRIS devices show an increased performance with SNR values of up to 4 dB better than an SOA.

In Fig. 7 the ASE output is shown when no input pulse train is present. As can be seen in the SOA the amplification of the generated spontaneous emission causes the output power to rise quickly, to over 1 mW at 150 mA injection current. The amplification of the SOAs in the IRIS devices is counterbalanced by the attenuation of the SAs, leading to a heavily decreased ASE power, i.e., about three orders of magnitude lower at the IRIS output facets. The difference between the ASE at the IRIS output and the (counter propagating) ASE emitting from the input side is explained by the fact that the IRIS configuration studied starts with an SOA at the input and ends with an SA at the output. We note that the ASE power at the output side can be decreased further when the small SOA sections at the output in the devices discussed here are omitted. This is more easily realized in an active-passive integration scheme, where no cleaving through the IRIS device is necessary [2].

The ASE suppression is only working up to the level where the total ASE power starts to saturate the SAs. This effect of SA saturation can be observed in the 60 μm/10 μm configuration. Starting from around 200–300 mA, an increase in ASE power is observed at the output facet.

Concluding it can be said that the IRIS devices perform better than an SOA of the same length with respect to picosecond pulse amplification. The SNR can be improved by about 4 dB and the ASE generation when no signal is present by over 30 dB. However maximum gain levels that can be achieved are higher for an SOA by up to 4 dB. Note that in this section we consider the pulse energy gain. The effects of pulse shaping and the corresponding effect on the pulse peak gain are discussed in the next section.

C. IRIS Time Domain Pulse Shaping

In the application for amplification of picosecond pulses we now want to compare the performance of the IRIS devices to an SOA with respect to pulse shaping in the time domain. The temporal pulse shaping in the IRIS devices has been studied using a 700-GHz optical sampling oscilloscope (Fig. 3). As the spectra obtained with the IRIS devices are smoother than those obtained with the SOA (Fig. 4), this can indicate an increased linearity of the chirp. This would make the output pulses more suitable for further compression using only second order dispersion, e.g., as present in SMF. In our setup the temporal output pulse shapes were measured after propagation through 15 m of SMF, with a total dispersion of 0.34 ps^2. This corresponds to a pulse broadening (or compression) value of approximately 0.3 ps per nanometer optical bandwidth, assuming linear chirp profiles. Given the optical bandwidths as mentioned in Fig. 4, this value of the dispersion will clearly lead to either pulse compression or broadening in our setup, depending on the sign of the chirp of the pulses.

In Fig. 8(a), the experimentally obtained temporal profiles of pulses amplified by 50 μm/10 μm and 40 μm/20 μm IRIS devices and by a 2 mm SOA are shown. For the SOA output it can be seen that partial pulse compression by the SMF takes place, resulting in a 1.3-ps peak with a pedestal that increases with increasing injection current. This effect is explained by the nonlinear chirp profile over the output pulse directly after the SOA due to its saturation.

Comparing the pulse shapes obtained with the IRIS devices with the ones obtained with the SOA, a severe decrease in the pulse pedestal is observed for increasing the SA length, having a bias voltage of -1 V. This effect is most pronounced for the

40 μm/20 μm device, which shows a pulse duration of 1.1 ps [Fig. 8(a)]. This duration is at the limit of the 700 GHz oscilloscope bandwidth. Decreasing the SA voltage down to -3 V reduces the pedestal even slightly more.

The model of Section III is then used to simulate the pulse shape directly at the IRIS output and after 15 m of SMF. The results are shown in Fig. 8(b) and (c). By comparing the simulated pulse shapes after 15 m of SMF with the experimentally obtained ones, we can state that there is agreement. A value of $N_{\mathrm{tr}} = 0.1 \cdot 10^{24}\ \mathrm{m}^{-3}$, which relates to an SA voltage of between -1 and -2 V, clearly reduces the pulse pedestal, just as observed in the experimental results. The simulated pulse shapes at the IRIS facet show that this decrease is a result of the limited temporal broadening due to the SA absorption. Moreover the simulation results show the possibility of obtaining pedestal free subpicosecond pulses. Directly at the IRIS facet a pulse duration of 0.6 ps is simulated for a 60 μm/40 μm device at $N_{\mathrm{tr}} = 0.5 \cdot 10^{24}\ \mathrm{m}^{-3}$ (a high reverse bias voltage). This is the relevant pulse duration when the IRIS device is integrated with further pulse processing components on the same chip. After 15 m of SMF a minimum value of 0.8 ps is simulated at $N_{\mathrm{tr}} = 0.3 \cdot 10^{24}\ \mathrm{m}^{-3}$. It has to be noted that the model used in the simulations has a limited validity to temporal pulse shapes down to around 1 ps. We note that the simulated pulse shapes obtained at $N_{\mathrm{tr}} = 0.6 \cdot 10^{24}\ \mathrm{m}^{-3}$ are low-power due to the increased absorption in the SAs and the SAs are driven into saturation less deeply. As a result the SOAs and SAs operate in a more linear regime and temporal pulse compression is decreased.

So concluding it can be said that in picosecond pulse amplification, the IRIS device shows a decreased temporal broadening and an increased linearity of the chirp at the output facet compared to an SOA. Consequently in combination with a second order dispersive element, the IRIS device shows better performance for compressing picosecond pulses. As such it is a promising candidate for further integration with mode-locked semiconductor lasers, which typically generate picosecond pulses and are often fiber coupled. The simulations show that increased compression is possible down to 0.6 ps, but this is beyond the resolution of our measurement equipment. It has to be noted that due to the relatively low peak power and the pulsed injection current it was not possible to obtain autocorrelator traces for reference.

V. Conclusion

In this work, we have presented a new device, named IRIS, which consists of a concatenated array of SOAs and SAs. We have experimentally and theoretically investigated picosecond pulse transmission through these devices. To this end we have first set up models to describe pulse propagation through a single SOA or SA section. These were validated experimentally to be able to describe picosecond pulse shaping, both temporally and spectrally, and ASE generation quantitatively. These models were then combined to simulate complete IRIS configurations. Depending on the design and operating conditions, the IRIS device can fulfill the role of a picosecond pulse amplifier, a temporal pulse shaper or a spectral shaper. Different device configurations have been realized.

As a spectral shaper the IRIS device shows improved spectral shaping of picosecond pulses as compared to an SOA of equivalent length. Spectral widths of over 5 nm can be obtained with a smooth shape. This makes the spectrum suitable for use in target applications where integrated AWGs are used [2], [27], [28]. The 5-nm bandwidth makes it possible to use over ten channels in high resolution InP AWGs.

With respect to the amplification of a picosecond pulse train it can be concluded that the achievable pulse energy gain is about 3 dB lower for the IRIS devices than for an SOA of equivalent length. The SNR for an IRIS device is up to 4 dB better. Moreover the experiments and the simulations demonstrate a decreased pulse broadening for the IRIS devices and even the possibility for pulse compression, from 1.4 ps down to 1.1 ps experimentally and 0.6 ps in the simulations. An increased linearity of the pulse chirp for the IRIS devices also suppresses the formation of a pulse pedestal. The absence of a pedestal makes the IRIS device more suitable for application in future high bit-rate OTDM networks. As a last important feature it has to be mentioned that the ASE generation when no input light is present is heavily suppressed in the IRIS devices as compared to SOAs, with suppression of up to 30 dB. As a drawback one has to mention that the IRIS devices generally operate at higher injection currents than SOAs of comparable size because of the inclusion of the SA sections.

The agreement between the simulated and experimental results obtained with the IRIS device and SOA makes our model a tool to identify design and operating issues and to optimize the IRIS design.

Concluding we can say that for picosecond pulse amplification and spectral shaping the IRIS configuration shows better performance than an SOA of equivalent length. As the fabrication process of the realized IRIS devices is compatible to the process to fabricate semiconductor mode-locked lasers, it is a promising option to integrate the two devices in order to either boost the pulse power or to increase the spectral bandwidth. Using active-passive integration further pulse processing components, e.g., AWG based, can be monolithically integrated.

References

[1] L. A. Jiang, E. P. Ippen, and H. Yokoyama, "Semiconductor mode-locked lasers as pulse sources for high bit rate data transmission," *J. Opt. Fiber. Commun. Rep. 2*, pp. 1–31, 2005.

[2] C. Ji, R. G. Broeke, Y. Du, J. Cao, N. Chubun, P. Bjeletich, F. Olsson, S. Lourdudoss, R. Welty, C. Reinhardt, P. L. Stephan, and S. J. B. Yoo, "Monolithically integrated InP-based photonic chip development for O-CDMA systems," *IEEE J. Sel. Topics Quantum Electron.*, vol. 11, no. 1, pp. 66–77, Jan./Feb. 2005.

[3] Th. Udem, R. Holzwarth, and T. W. Hänsch, "Optical frequency metrology," *Nature*, vol. 416, pp. 233–237, Mar. 2002.

[4] K. Takiguchi, K. Okamoto, T. Kominato, H. Takahashi, and T. Shibata, "Flexible pulse waveform generation using silica-waveguide-based spectrum synthesis circuit," *Electron. Lett.*, vol. 40, no. 9, pp. 537–538, 2004.

[5] R. Kaiser, B. Hüttl, H. Heidrich, S. Fidorra, W. Rehbein, H. Stolpe, R. Stenzel, W. Ebert, and G. Sahin, "Tunable monolithic mode-locked lasers on InP with low timing jitter," *IEEE Photon. Technol. Lett.*, vol. 15, no. 5, pp. 634–636, May 2003.

[6] K. Yvind, L. J. Christiansen, C. Angelo, L. K. Oxenløwe, J. Mørk, D. Birkedal, J. M. Hvam, and J. Hanberg, "Low-jitter and high-power 40-GHz all-active mode-locked lasers," *IEEE Photon. Technol. Lett.*, vol. 16, no. 4, pp. 975–977, Apr. 2004.

[7] Y. Barbarin, E. A. J. M. Bente, M. J. R. Heck, J. H. den Besten, G. Guidi, Y. S. Oei, J. J. M. Binsma, and M. K. Smit, "Realization and modeling of a 27-GHz integrated passively mode-locked ring laser," *IEEE Photon. Technol. Lett.*, vol. 17, no. 11, pp. 2277–2279, Nov. 2005.

[8] Y. Barbarin, E. A. J. M. Bente, M. J. R. Heck, Y. S. Oei, R. Nötzel, and M. K. Smit, "Passively modelocked 20 and 40 GHz bulk InGaAsP lasers," in *Proc. Eur. Conf. Opt. Commun. (ECOC)*, Glasgow, UK, 2005, pp. 673–674.

[9] Y. Barbarin, E. A. J. M. Bente, M. J. R. Heck, Y. S. Oei, R. Nötzel, and M. K. Smit, "Characterization of a 15 GHz integrated bulk InGaAsP passively modelocked ring laser at 1.53 μm," *Opt. Exp.*, vol. 14, no. 21, pp. 9716–9727, 2006.

[10] M. J. R. Heck, E. A. J. M. Bente, Y. Barbarin, D. Lenstra, and M. K. Smit, "Monolithic semiconductor waveguide device concept for picosecond pulse amplification, isolation and spectral shaping," *IEEE J. Quantum Electron.*, vol. 43, no. 10, pp. 910–922, Oct. 2007.

[11] J. M. Tang and K. A. Shore, "Amplification of strong picosecond optical pulses in semiconductor optical amplifiers," *Proc. IEE Optoelectron.*, vol. 146, pp. 45–50, Feb. 1999.

[12] R. Gutiérrez-Castregón, L. Schares, L. Occhi, and G. Guekos, "Modeling and measurement of longitudinal gain dynamics in saturated semiconductor optical amplifiers of different length," *IEEE J. Quantum Electron.*, vol. 36, no. 12, pp. 1476–1484, Dec. 2000.

[13] G. Talli and M. J. Adams, "Gain dynamics of semiconductor optical amplifiers and three-wavelength devices," *IEEE J. Quantum. Electron.*, vol. 39, no. 10, pp. 1305–1313, Oct. 2003.

[14] M. Willatzen, A. Uskov, J. Mørk, H. Olesen, B. Tromborg, and A.-P. Jauho, "Nonlinear gain suppression in semiconductor lasers due to carrier heating," *IEEE Photon. Technol. Lett.*, vol. 3, no. 7, pp. 606–609, Jul. 1991.

[15] J. Huang and L. W. Casperson, "Gain and saturation in semiconductor lasers," *Opt. Quantum Electron.*, vol. 25, pp. 369–390, 1993.

[16] M. J. R. Heck, E. A. J. M. Bente, Y. Barbarin, D. Lenstra, and M. K. Smit, "Simulation and design of integrated femtosecond passively mode-locked semiconductor ring lasers including integrated passive pulse shaping components," *IEEE J. Quantum Electron.*, vol. 12, no. 2, pp. 265–276, Mar./Apr. 2006.

[17] R. G. M. P. Koumans and R. van Roijen, "Theory for passive mode-locking in semiconductor laser structures including the effects of self-phase modulation, dispersion and pulse collisions," *IEEE J. Quantum Electron.*, vol. 32, no. 3, pp. 478–492, Mar. 1996.

[18] Y. Barbarin, E. A. J. M. Bente, M. J. R. Heck, J. Pozo, J. M. Rorison, Y. S. Oei, R. Nötzel, and M. K. Smit, "18 GHz Fabry-Pérot integrated extended cavity passively modelocked lasers," Proc. ECIO 2007 Apr. 2007, Paper ThG07.

[19] U. Bandelow, M. Radziunas, A. Vladimirov, B. Hüttl, and R. Kaiser, "40 GHz mode-locked semiconductor lasers: Theory, simulations and experiment," *Opt. Quantum Electron.*, vol. 38, no. 4–6, pp. 495–512, Mar. 2006.

[20] R. P. Schreieck, "Ultrafast dynamics in InGaAsP/InP optical amplifiers and mode locked laser diodes," Ph.D. dissertation, Swiss Federal Inst. Technol. Zurich, Switzerland, 2001.

[21] F. Romstad, F. Öhman, J. Mørk, K. Yvind, J. M. Hvam, and J. Hanberg, "Short pulse absorption dynamics in a p-i-n InGaAsP MQW waveguide saturable absorber," in *Proc. ECOC 2002*, Sep. 8–12, 2002, p. 2.25.

[22] F. Girardin and G. Guekos, "Gain recovery of bulk semiconductor optical amplifiers," *IEEE Photon. Technol. Lett.*, vol. 10, no. 6, pp. 784–786, Jun. 1998.

[23] Y. Barbarin, E. A. J. M. Bente, G. Servanton, L. Mussard, Y. S. Oei, R. Nötzel, and M. K. Smit, "Gain measurements of Fabry–Perot InP–InGaAsP lasers using an ultrahigh-resolution spectrometer," *Appl. Opt.*, vol. 45, no. 35, pp. 9007–9012, Dec. 2006.

[24] J. Mørk, J. Mark, and C. P. Seltzer, "Carrier heating in InGaAsP laser amplifiers due to two-photon absorption," *Appl. Phys. Lett.*, vol. 64, no. 17, pp. 2206–2208, Apr. 1994.

[25] D. J. Jones, L. M. Zhang, J. E. Carroll, and D. D. Marcenac, "Dynamics of monolithic passively mode-locked semiconductor lasers," *IEEE J. Quantum Electron.*, vol. 31, no. 6, pp. 1051–1058, Jun. 1995.

[26] J. R. Karin, R. J. Helkey, D. J. Derickson, R. Nagarajan, D. S. Allin, J. E. Bowers, and R. L. Thornton, "Ultrafast dynamics in field-enhanced saturable absorbers," *Appl. Phys. Lett.*, vol. 64, no. 6, pp. 676–678, Feb. 1994.

[27] M. J. R. Heck, P. Muñoz, E. A. J. M. Bente, Y. Barbarin, D. Lenstra, and M. K. Smit, "Simulation and design of integrated pulse shaping components for femtosecond modelocked ring lasers," *Proc. ECIO*, pp. 351–354, Apr. 2005.

[28] H. Tsuda, K. Okamoto, T. Ishii, K. Naganuma, Y. Inoue, H. Takenouchi, and T. Kurokawa, "Second- and third-order dispersion compensator using a high-resolution arrayed-waveguide grating," *IEEE Photon. Technol. Lett.*, vol. 11, no. 5, pp. 569–571, May 1999.

[29] F. Öhman, S. Bischoff, B. Tromborg, and J. Mørk, "Noise and regeneration in semiconductor waveguides with saturable gain and absorption," *IEEE J. Quantum Electron.*, vol. 40, no. 3, pp. 245–255, Mar. 2004.

[30] L. J. Christiansen, L. Xu, K. Yvind, F. Öhman, L. Oxenløwe, and J. Mørk, "2R regeneration in concatenated semiconductor optical amplifier and electroabsorbers," in *Proc. Eur. Conf. Optical Commun. (ECOC)*, Stockholm, Sweden, 2004, pp. 30–31.

Martijn J. R. Heck (S'04) was born in Nijmegen, The Netherlands, in 1976. He received the M.Sc. degree in applied physics from Eindhoven University of Technology, Eindhoven, The Netherlands, in 2002. He is currently working toward the Ph.D. degree in the Opto-Electronic Devices group of the COBRA Research Institute, Eindhoven University of Technology, The Netherlands, where he is involved in research on integrated ultrafast semiconductor technology.

His masters thesis work was carried out at ASM Lithography, The Netherlands, on the characterization of processed optical alignment marks on semiconductor wafers using an atomic force microscope.

Ervin A. J. M. Bente (M'01) received the M.Sc. degree in physics and the Ph.D. degree from Vrije Universiteit, Amsterdam, The Netherlands, in 1983 and 1989, respectively. His thesis work was on atomic laser spectroscopy.

From 1988 to 1994, he was with Urenco Nederland B.V. and led a research group on laser isotope separation. From 1994 to 1996, he was with Vrije Universiteit in Amsterdam as a Researcher working on solid-state coherent light sources and isotope separation of stable isotopes. He worked as a Research Team Leader at the Institute of Photonics, University of Strathclyde, Glasgow, U.K., involved in high-power diode-pumped solid-state lasers, passive modelocking, and femtosecond laser machining. In 2001, he moved to the COBRA Research Institute, Eindhoven University of Technology, Eindhoven, The Netherlands, where he now an Associate Professor and is working on integrated semiconductor laser systems.

Dr. Bente is a member of the Institute of Physics and the Optical Society of America.

Yohan Barbarin (S'03) received the M.Sc. degree in 2002 from the Marseille National Higher School in physics and engineering (ENSPM), Marseille, France, now "Centrale Marseille." He is currently working toward the Ph.D. degree at the COBRA Research Institute at Eindhoven University of Technology, The Netherlands with research concerning the development of integrated mode-locked semiconductor laser sources for 160–640 Gbit/s optical time-domain multiplexed (OTDM) applications.

He is currently working as a Researcher at ETH Zürich, Switzerland on electrically pumped mode-locked vertical extended cavity surface emitting lasers (VECSELs).

Antigoni Fryda (S'06) was born in Amarousio Attikis, Greece, in 1984. She is currently working towards the M.Sc. degree in electrical engineering at the Aristotle University, Thessaloniki, Greece.

In 2005-2006, she was with the Opto-Electronic Devices group of the COBRA Research Institute, Eindhoven University of Technology, The Netherlands, where she was involved in research on integrated pulse shaping devices.

Hyun-Do Jung received the B.S. degrees in radio sciences and engineering from Kyunghee University, Kyunghee, Korea, in 1999, and the Ph.D. degree in electrical and electronic engineering from Yonsei University, Yonsei, Korea, in 2005.

Since 2005, he has been with the Department of Electrical Engineering, Eindhoven University of Technology, The Netherlands, as a Postdoctoral Researcher where he is involved in research on optical packet switching. His current research interests include optical systems for communications, optical packet switching, and microwave photonics technologies.

Yok-Siang Oei is an Associate Professor at the Department of Electrical Engineering of the Eindhoven University of Technology, The Netherlands.

Within the COBRA Research Institute, he is responsible for the development of the fabrication technology of InP-based devices. He is working on the monolithic integration of photonic devices. He is author and coauthor of more than 150 journal and conference papers.

Richard Nötzel is an Associate Professor in the Photonics and Semiconductor Nanophysics group of Eindhoven University of Technology, Eindhoven, The Netherlands.

He has a broad background in the MBE, CBE, and MOVPE growth of low-dimensional semiconductors and their electronic properties for applications in monolithically integrated photonic devices. He is (co) author of more than 240 publications in peer reviewed Journals and International Conferences, including more than 30 invited talks.

Dr. Nötzel received many awards such as the Otto Hahn medal of the Max-Planck society, the research award from the NTT Opto-electronics Laboratories, and the academy award of the Berlin-Brandenburg Academy of Science.

Daan Lenstra (SM'06) was born in Amsterdam, The Netherlands, in 1947. He received the M.Sc. degree in theoretical physics from the University of Groningen, Groningen, The Netherlands, in 1972, and the Ph.D. degree from Delft University of Technology, Delft, The Netherlands, in 1979. His thesis work was on polarization effects in gas lasers.

Since 1979, he has researched topics in quantum electronics, laser physics, and condensed matter physics. In 1991, he joined Vrije Universiteit, Amsterdam, The Netherlands, holding a Chair in Theoretical Quantum Electronics. From 2000 to 2006, he was also with COBRA Research Top Institute, Eindhoven University of Technology, where he occupied the chair of Ultrafast Photonics. He was Scientific Director of COBRA from 2004 to 2006. His research themes are nonlinear and ultra-fast dynamics of semiconductor optical amplifiers and diode lasers, quantum optics in small semiconductor structures, and near-field optics. Since November 2006, he has been the Dean of the Faculty of Electrical Engineering, Mathematics and Computer Science of Delft University of Technology. He has (co)authored more than 300 publications in international scientific journals and (co) edited 6 books and several special journal issues.

Dr. Lenstra is senior member of IEEE LEOS, member of OSA and EPS and acts regularly as program (co)chair for international meetings.

Meint K. Smit (F'03) received the M.Sc. (hons) and Ph.D. (hons) degrees in electrical engineering from Delft University of Technology, Delft, The Netherlands, in 1974 and 1991, respectively.

In 1974, he started work on radar and radar remote sensing, and joined Delft University of Technology in 1976. He became leader of the Photonic Integrated Circuits Group, Delft University, in 1994, and was appointed Professor in 1998. In 2002, he moved with the Photonic Integrated Circuits Group to Eindhoven University, University of Technology, Eindhoven, The Netherlands, where he is presently the Leader of the Opto-Electronic Devices group of the COBRA Research Institute.

Dr. Smit is the inventor of the arrayed waveguide grating, for which he received a LEOS Technical Award in 1997. Also in 1997, the Photonic Integrated Circuits Group, along with the Semiconductor Materials Group under Prof. Wolter and the Communication Systems Group under Prof. Khoe, received a research grant to establish the National Research Center on Photonics. He became a Fellow of the IEEE Lasers and Electro-Optics Society in 2002 for contributions in the field of opto-electronic integration.